Star identification robust to angular rates and false objects with rolling shutter compensation

Vincenzo Schiattarella[1,]

Sapienza University of Rome, School of Aerospace Engineering - ARCAlab

Dario Spiller[2]

Sapienza University of Rome, School of Aerospace Engineering - ARCAlab

Fabio Curti[3]

Sapienza University of Rome, School of Aerospace Engineering - ARCAlab

Abstract

This paper addresses the problem of star identification in the presence of high slew rates, false objects and image deformations introduced by the rolling shutter. These problems can affect the operating life of star trackers and worsen the nominal performances. The proposed methodology relies on a technique named Improved Multi-Poles Algorithm, especially designed for robustness to false objects and slew rates. Angular velocities up to five degrees per second are considered so that stars are seen no more as near-circular spots but appear as streaks. The image deformation due to the rolling shutter of modern active pixel sensor detectors is compensated by means of a mathematical model based on a first order approximation of the problem. A star tracker high fidelity simulator generates the input images considering typical noises due to the electronics and space environment. The reported results show that the proposed approach guarantees a reliable star identification and attitude determination with angular velocity from zero to five degrees per second.

Email addresses: vincenzo.schiattarella@uniroma1.it (Vincenzo Schiattarella), dario.spiller@uniroma1.it (Dario Spiller), fabio.curti@uniroma1.it (Fabio Curti)

[1]Research assistant. Addr.: Via Salaria 851, 00138 Rome Italy

[2]Ph.D. Addr.: Via Salaria 851, 00138 Rome Italy

[3]Associate Professor. Addr.: Via Salaria 851, 00138 Rome Italy

Keywords: star tracker, false objects, slew rate, lost in space, rolling shutter, attitude determination

1. Introduction

Star trackers are accurate devices capable of determining the spacecraft's attitude within the magnitude of arc-seconds without any a priori information [1]. Nowadays, star trackers are necessary instruments of the navigation subsystem of a satellite, thanks to their measurement accuracy along with their more and more reduced dimensions with the technological advances of the recent years [2]. In Lost In Space (LIS) mode, i.e. when the attitude is unknown, the star tracker's camera provides images of an unknown region of the sky to the on-board processor. Here, a star identification algorithm recognizes the visible stars in the images by using a star catalog stored on-board [3]. All the methods for the identification of detected stars are based on the evaluation of some geometric patterns that are related to the relative positions of the stars, e.g. triangles [1, 4, 5], polygons [6], pyramids [7] or grids [8, 9, 10]. Some approaches identify the detected stars by evaluating the angular distances of all the stars from a single selected one, defined as the pole of the image [11, 12, 13].

This paper deals with the star identification problem in LIS mode when the star tracker is supposed to compensate for the combined presence of slew rates and false objects.

Slew rates significantly decrease the signal-to-noise ratio (SNR) so that the accuracy of the centroids extracted from the detected image is reduced. Pioneering studies are reported in [14], where the Liebe model of the signal left by a star on the detector is presented as a function of the angular velocity. In [15] a comparison of the Liebe model and the Reed model is shown, and simulated images are created taking into account the dispersion of the star signal over *streaks* due to the angular velocity. In fact, the signal left by the stars over the single pixel diminishes, and faint stars disappear as they can get confused with the surrounding noise [16]. Pre-processing and centroiding operations under dynamic conditions are taken into account in [17]. Attitude accuracy depends on the number of detected stars and how precisely the centroids of these stars are determined. Hence, even though star trackers generally have arc-second accuracy in stationary conditions, their performances usually degrade as slew rate increases.

A further problem related to slew rates appears for those star trackers that use a detector with rolling shutter, usually active pixel sensors (APS). In this case, it is well known that the detected image is deformed and it does not appear as expected. The APS deformation affects the star tracker operations since the centroids are not related to the same time instant. In the frame of this paper, a deformation model based on preliminary analyses reported in [16, 18] is presented. By using a first order approximation of the real motion of the stars across the detector, the proposed strategy is used to set the centroids to the same time instant.

The use of star trackers in harsh environments, characterized by a great number of Single Event Upset (SEU), is potentially limited due to the star identification sensitivity to false objects [19]. Generally, the star identification algorithms are poorly robust to false spikes. In [20] a method is presented to successfully manage a number of false objects up to 3 times the number of the cataloged stars when the spacecraft is in a fixed attitude. In [21] a three phases technique, the Multi-Poles Algorithm (MPA) is introduced. It is demonstrated that correct identifications are evaluated for 100% of the simulations, even when the number of false objects is up to 6 times the number of the cataloged stars detected in the image.

A modified and improved version of the MPA has been developed to participate at Kelvins ESA contest - Star Trackers: First Contact [4], where the MPA has reported the second highest accuracy score and speed [22].

An updated and more efficient version of the MPA is proposed in this paper and referred to as the Improved MPA (IMPA). The identification feature is the angular distance between two stars. Stars' magnitudes are used as a filtering feature to improve the searching strategy. Due to magnitude filtering, stars may be identified using only two phases, therefore simplifying the algorithm architecture. The *acceptance phase* yields an initial set of stars, followed by the *check phase* in order to avoid erroneous identifications. The first phase uses a polar technique to provide a set of accepted stars (pole and neighbor stars). Then, taking a previous neighbor star as the new pole, a new accepted stars set is provided by a second run of the acceptance phase. Finally, the check phase checks the number of stars belonging to both the two sets of accepted stars. When using a detector based on rolling shutter,

[4] http://kelvins.esa.int/star-trackers-first-contact (from the 1st September 2016 to the 1st September 2017)

the robustness to slew rates has been increased by using the aforementioned compensation model and setting all the stars' centroids to the same time instant. The algorithm is tested when the spacecraft experiences an angular velocity in the range of 0-5 deg/sec.

To sum up, the main contributions of this paper are:

- The development of a mathematical model to compensate for the rolling shutter deformation.
- The development of the IMPA based on the introduction of a magnitude filtering.
- The numerical demonstration that reliable and accurate results are obtained using state-of-the-art detectors and the rolling shutter compensation combined with the IMPA.

The paper is organized as follows. In Sec. 2 some preliminary concepts related to the star tracker operations are described. In Sec. 3 the description of the rolling shutter effects is given in the presence of angular rates and in Sec. 4 the analyses of the stars distribution and detection as a function of the angular velocity is reported. In Sec. 5 the proposed star recognition algorithm is explained. In Sec. 6 the simulations results are showed and in Sec. 7 conclusions and final remarks are reported.

2. Preliminary processing of the image

In this section a description of the image processing is given. The following details are given to fully understand the successive sections, where the concepts and operations herein described will be considered as operational tools. The cluster fusion procedure is introduced for the compensation of the rolling shutter deformation described in Sec. 3.2.

2.1. Preprocessing

The high-energy pixels belonging to the star signals must be distinguished from the low-energy pixels where only noise is recorded. Accordingly, an image preprocessing selects the pixels whose signal-to-noise ratio (SNR) is greater than a user-defined detection threshold and discards the other ones [23]. This preliminary operation is referred to as segmentation and it is usually performed using a run-length encoding algorithm [24].

The segmentation algorithm can be implemented using a static (global) or a dynamic (local) approach [17]. The SNR is evaluated considering the same background noise for the static approach and a specific background noise for each pixel of the detector for the dynamic approach. A survey of different techniques is reported in [25]. In this work, a zigzag local thresholding using moving averages is used [26]. Hence, the only pixels that are considered for further investigations are those with values greater than the background level (evaluated with moving average) plus a threshold τ_{pre}. It is noteworthy that quantization errors can occur due to pixel discretization of the image.

The outputs of the preprocessing operation are the selected pixels' coordinates $\boldsymbol{p} = [p_y, p_z]^T$ and their energy $E(\boldsymbol{p})$, obtained subtracting the background level to the entire signal intensity of the pixel.

2.2. Clustering

Because the energy of a detected object is spread out over several close pixels, a clustering technique merges those pixels in a cluster $\mathscr{C}$ and removes isolated pixels from the image. The centroid $\boldsymbol{c}_i = [c_{y,i}, c_{z,i}]^T$ is the reference position of the i^{th} cluster $\mathscr{C}_i$ and it is computed using coordinates and energies of the pixels belonging to it, throughout an energy-weighted average, i.e.

$$\boldsymbol{c}_i = \frac{1}{E_{\mathscr{C}_i}} \sum_{j|\boldsymbol{p}_j \in \mathscr{C}_i} E(\boldsymbol{p}_j) \cdot \boldsymbol{p}_j, \tag{1}$$

where $E(\boldsymbol{p}_j)$ is the (in electrons e^-) of the pixel $\boldsymbol{p}_j$ and

$$E_{\mathscr{C}_i} = \sum_{j|\boldsymbol{p}_j \in \mathscr{C}_i} E(\boldsymbol{p}_j) \tag{2}$$

is the total energy of the i^{th} cluster.

2.3. Cluster Fusion

The cluster fusion is required to compare two successive images. For detectors with rolling shutter, this operation evaluates some essential information for the compensation of the induced deformation. Moreover, regardless of the detector's technology, the fusion evaluates information generally required for stars tracking once the lost in space phase is accomplished. Indeed, one output of the fusion is the velocity of the centroids' focal plane, and this information can be used to guess the position of the stars when operating

in tracking mode. Clusters of fixed stars can appear as moving objects if the satellite is rotating. Let two successive images be considered, respectively with $N_{c,1}$ and $N_{c,2}$ detected clusters. In order to merge the clusters from two successive images, the following procedure is used:

1. The cluster $\boldsymbol{c}_i$ is considered in the first image, with $1 \leq i \leq N_{c,1}$.
2. The cluster $\boldsymbol{c}_j$, $1 \leq j \leq N_{c,2}$, which has the minimum distance with respect to $\boldsymbol{c}_i$ is searched in the second image. This operation is carried out looking at the pixel-to-pixel distance in order to be independent from the angular rate magnitude.
3. If the distance between $\boldsymbol{c}_i$ and $\boldsymbol{c}_j$ is less than a user-defined threshold d_f, then the two clusters are merged. Using the centroids' coordinates, the sign of the velocity is evaluated as

$$s_y = \text{sign}\left(\frac{c_{y,i} - c_{y,j}}{T_{exp}}\right), \quad s_z = \text{sign}\left(\frac{c_{z,i} - c_{z,j}}{T_{exp}}\right). \tag{3}$$

4. All the clusters for which a feasible distance is not found are discarded.

It is noteworthy that Eq. (3) estimates only the sign of the velocity components in the focal plane $\{\boldsymbol{y}_{\mathcal{F}}, \boldsymbol{z}_{\mathcal{F}}\}$ from a couple of successive images.

3. Rolling shutter and global shutter

In this section the global and the rolling shutter acquisition models are compared. The deformation introduced by the rolling shutter is mathematically modeled and a first-order compensation strategy is presented.

3.1. Acquisition models

Let the detector be composed by n_{row} rows and n_{col} columns. Fig. 1 reports the detection profile of two successive images using a sensor with global shutter. The first image acquisition starts at time t_0. For all the rows of the detector, the exposure begins at time t_0 and finishes after a time interval denoted as T_{exp}. At time $t_1 = t_0 + T_{exp}$ the first image acquisition ends and it can be read-out. Fig. 1 reports the case of an image read from the sensor while the next one is being exposed. This is possible for many image sensors with global shutter because they have extra storage for each pixel (each pixel can store its value on the previous image while the next one is being exposed). At time t_1 the second image acquisition starts. In accordance with the first image, the second acquisition ends at time $t_2 = t_1 + T_{exp}$.

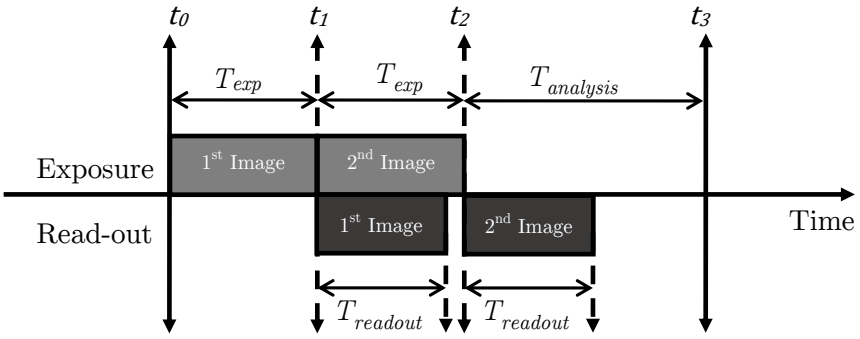

Figure 1: Acquisition architecture with global shutter.

For a detector with rolling shutter, the image is progressively acquired row by row. The detection profile of a sensor with rolling shutter is represented in Fig. 2. The reset and read-out operation of each row requires an amount of time equal to t_l (line time). For star trackers, it is desirable to have the highest frame rate as possible, in order to reduce latency in attitude determination and motion blur (when the spacecraft is rotating). However, the frame rate is limited by two factors: the minimum exposure time needed to detect a sufficient number of stars that provides a good sky coverage (high probability of attitude acquisition, given an initial random attitude) and the minimum time needed to read the image sensor (read-out time). Assuming that the minimum exposure time needed for attitude acquisition is shorter than the image read-out time (typically of the order of tens or hundreds of milliseconds), there is little benefit in setting the exposure time to values shorter than the image read-out time, since the frame rate will already be limited by the image read-out time. According to this observation, the exposure time is defined as

$$T_{exp} = t_l \cdot n_{row}. \tag{4}$$

It should be noted that this equation is not always true, since the exposure time does not necessarily have to be defined as in the aforementioned equation. However, this equation could be considered valid in a simplified model of a star tracker. Hence, the first image acquisition starts at time t_0 (which

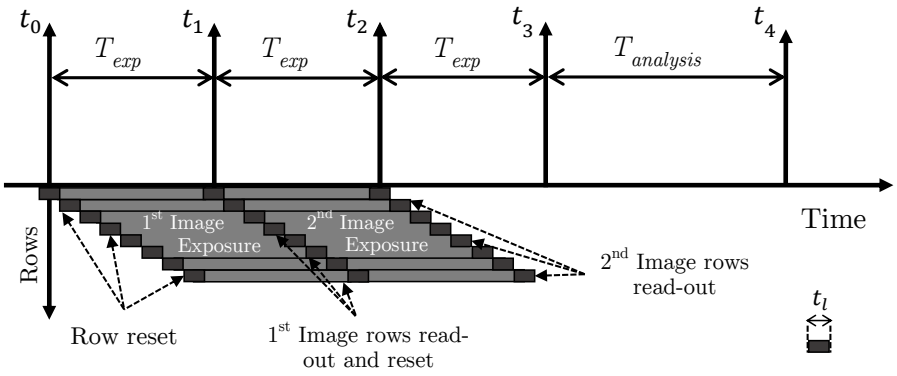

Figure 2: Acquisition architecture with rolling shutter.

can be considered approximately in the middle of the time interval t_l) and finishes at time $t_1 = t_0 + T_{exp}$. The exposure interval for the successive rows of the detector is given as

- $[t_0 + t_l, t_1 + t_l]$ for the second row,
- $[t_0 + 2t_l, t_1 + 2t_l]$ for the third row, and
- $[t_0 + (n-1)t_l, t_1 + (n-1)t_l]$ for the nth row.

Therefore, the last row exposure ends at time $t_1 + (n_{row} - 1)t_l$, and the whole detector image is available at time $t_2 = t_1 + n_{row}t_l = t_0 + 2T_{exp}$. However, when the first row has finished its exposure, the acquisition of the second image can start. Following the same reasoning as before and referring to Fig. 2, the second image is available at time $t_3 = t_0 + 3T_{exp}$.

3.2. Rolling shutter deformation compensation

The rolling shutter is typical of many active pixel sensor (APS) detectors and introduces a deformation in the detected image which can affect the results of the star identification process. Some models of the deformation compensation have been proposed in literature. For instance, in [27] a convolutional neural network architecture is used to automatically learn essential scene features from a single image. The rolling shutter distortions are then compensated and the whole image is referred to the time of the first-row exposure. In [28] a simple approach to the analysis of inter- and

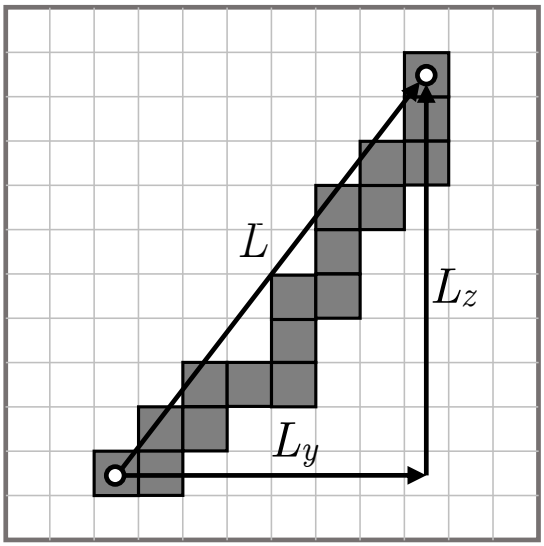

Figure 3: Definition of the streak length related to the star displacement.

intra-frame distortions is presented. The velocity estimates used for restoring the image are obtained by global motion estimation, Bèzier curve fitting and local motion estimation without resorting to correspondence identification. However, to the best of the authors' knowledge, simple models developed for star trackers have not yet been considered.

The method presented in this paper requires two successive images to understand the direction of the velocity, as explained in Sec. 2.3. Nevertheless, the estimate of the correction is independently evaluated for each streak based on topological information gained from a single image. Accordingly, a local and lightweight compensation is attained. The method is based on the rolling shutter deformation analysis of [16, 18].

As a consequence of the spacecraft angular velocity $\boldsymbol{\omega}$, stars will be detected as moving objects on the detector and, eventually, they will appear as streaks instead of circular spots.

Let v_y and v_z be the velocity components of the stars on the focal plane. Moreover, let L_y and L_z be the projections along y and z of the star streak's length, which is related to the displacement of the star as shown in Fig. 3. Hence, by considering a constant velocity during the exposure time, the

following equations holds,

$$T = \frac{L_y}{v_y} = \frac{L_z}{v_z}. \tag{5}$$

The mathematical model presented in this section is based on the schematic representation reported in Fig. 4 and is valid for the star considered as a single point. If the spot diameter is considered, the model becomes more complicated. However, the estimation of the spot diameter from the star streak is quite complicated since it depends on the star's magnitude and velocity. Both in Fig. 3 and Fig. 4 it is assumed that the star is detected from the center of the first row and arrives at the center of the last row. Moreover, in Fig. 4 the time axis has been conveniently translated in order to simplify the figure and T_{row} is denoted as the time required to cross one single row, i.e.

$$T_{row} = \frac{p}{v_z}. \tag{6}$$

In the following equations, k_0 and k_f will respectively denote the first and the last row belonging to a star streak, where first and last are meant in the direction of $z_{\mathcal{F}}$. Hence, the quantity Δk is defined as the difference between first and last row, i.e

$$\Delta k = k_f - k_0. \tag{7}$$

In Fig. 4, the vertical displacement d_z (expressed in pixel) of the star within each covered row is reported. As already stated, the star starts from 0.5 pixel in the first row and arrives at 0.5 pixel in the last row.

Let a star moving in the direction of the rolling shutter be considered, as shown in Fig. 4a. When the star is in the last row, the following equation holds,

$$\Delta k \cdot t_l + T_{exp} = \Delta k \cdot T_{row} \tag{8}$$

and the value of Δk can be evaluated as

$$\Delta k = \frac{T_{exp}}{T_{row} - t_l}. \tag{9}$$

Without loss of generality, let the detector be composed by square pixels with side p. The length of the star streak produced by the star is given by

$$L_z = p\Delta k. \tag{10}$$

As can be seen, the value of Δk from Eq. (9) is positive when $T_{row} \in (t_l, T_{exp}]$.

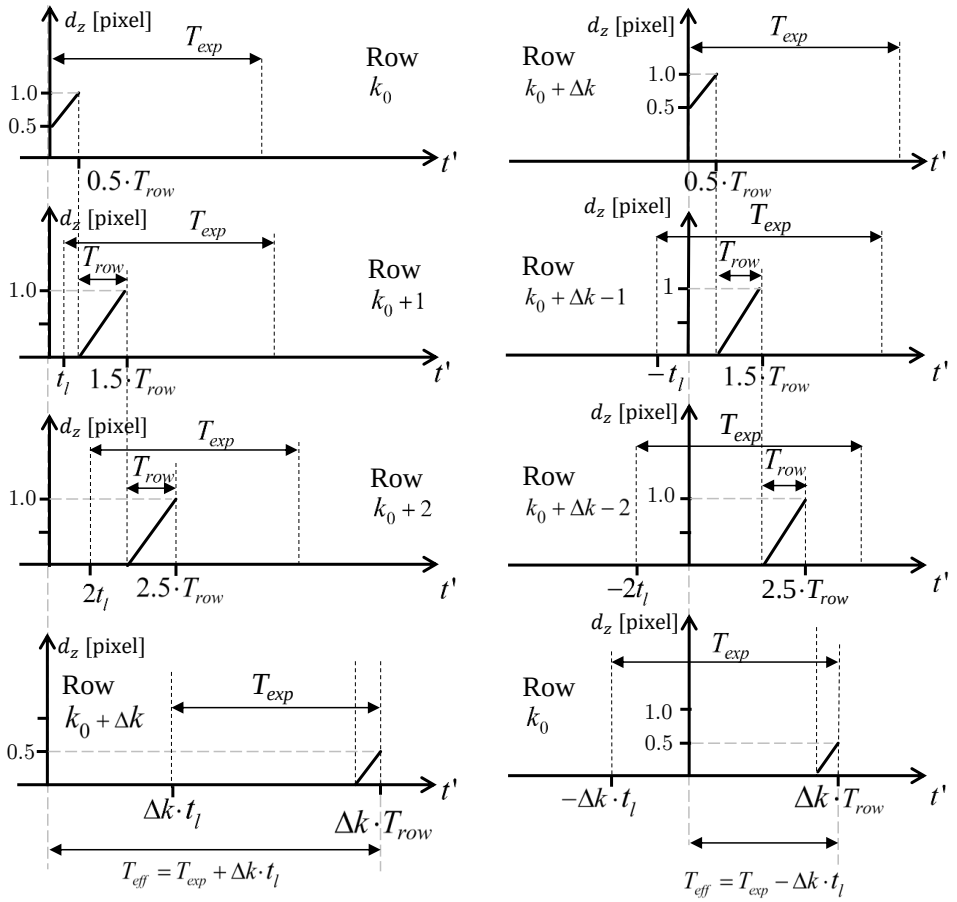

(a) (b)

Figure 4: Displacement of a star moving in the direction of the rolling shutter (a) with $t' = t - t_l k_0$ and in the opposite direction of the rolling shutter (b) with $t' = t - t_l(k_0 + \Delta k)$.

Indeed, if $T_{row} \geq T_{exp}$ the star cannot produce a streak longer than p and can be related at most to two rows (depending on the initial star's position within the first row). Applying Eq. (5), (6) and (10) for the effective exposure time T_{eff}, v_z can be computed as

$$v_z = v_z^+ = \frac{p\Delta k}{T_{row}\Delta k} = \frac{L_z}{T_{exp} + \Delta T} \tag{11}$$

where $T_{row}\Delta k$ can be evaluated from Eq. (8) and consequently

$$\Delta T = \Delta k t_l. \tag{12}$$

The notation v_z^+ is used to emphasize that the star is moving in the direction of the rolling shutter. It is noteworthy that in this model the value of v_z represents the mean value of velocity during the whole exposure. If the star is moving along the $y_{\mathcal{F}}$ direction, the norm of the velocity v_y is evaluated as

$$v_y^+ = \frac{L_y}{T_{exp} + \Delta T} \tag{13}$$

since the time on the detector is the same as for Eq. (11). Depending on the direction of the star along the $y_{\mathcal{F}}$ direction, $v_y = \pm v_y^+$.

Following the same reasoning as before and referring to Fig. 4b, it can be shown that the velocities v_y^- and v_z^- for a star moving in the opposite direction of the rolling shutter are computed as

$$v_z^- = \frac{L_z}{T_{exp} - \Delta T}\,, \tag{14}$$

$$v_y^- = \frac{L_y}{T_{exp} - \Delta T}\,, \tag{15}$$

where ΔT is defined as in Eq. (12). In this case, $v_z = -v_z^-$ and $v_y = \pm v_y^-$ depending on the direction of the star along the $y_{\mathcal{F}}$ direction.

Using Eq. (3), the sign of the star velocity with respect to $\{\boldsymbol{y}_{\mathcal{F}}, \boldsymbol{z}_{\mathcal{F}}\}$ can be introduced in the previous formulation and a more compact form of v_y and v_z is obtained as

$$v_z = \frac{L_z}{T_{exp} + s_z \Delta T}\,, \tag{16}$$

$$v_y = \frac{s_y L_y}{T_{exp} + s_z \Delta T}. \tag{17}$$

When $\Delta k = 0$, the minimum value of v_z is attained, i.e. $v_{z,min} = 0$. The proposed compensation scheme is accurate when the length of the star streak is long enough to make the star's spot dimension negligible. Considering a real star tracker, both the preprocessing segmentation and the instrumental

noises make the compensation reliable as long as v_y and v_z are greater than a user-defined threshold v^* which depends on the hardware characteristics.

The problem related to attitude determination algorithms when using APS with rolling shutter is the following: each streak is related to different time intervals depending on their position on the detector. Indeed, each streak is detected in the time interval

$$t \in [t_0, t_0 + T_{exp} + \Delta T] \qquad \text{with } t_0 = k_0 t_l, \text{ if } v_z \geq 0, \text{ or} \tag{18}$$

$$t \in [t_0, t_0 + T_{exp} - \Delta T] \qquad \text{with } t_0 = (k_0 + \Delta k) t_l, \text{ if } v_z < 0. \tag{19}$$

Accordingly, the centroids of the streaks cannot be used unless a correction is performed to set the centroids to the same time instant. Let $\boldsymbol{c}$ and $\tilde{\boldsymbol{c}}$ be the centroid position before and after the correction, respectively. A linear model can be developed on the basis of the previous estimates of v_y and v_z such that

$$\tilde{c}_y = c_y + \varepsilon_y(v_y), \quad \tilde{c}_z = c_z + \varepsilon_z(v_z)\,. \tag{20}$$

To minimize the errors, the reference time instant for each image is chosen as the time instant corresponding to half of the total detector exposure. In this way, the maximum error will be proportional to $0.5\,T_{exp}$. In fact, the time distance between two centroids is proportional to their vertical distance counted as number of rows. The linear expressions for ε_y and ε_z are

$$\varepsilon_y = v_y \Delta T^*, \quad \varepsilon_z = v_z \Delta T^*, \tag{21}$$

where

$$\Delta T^* = t_l \left(\frac{n_{row}}{2} - \tilde{c}_z \right). \tag{22}$$

4. Stars distribution and detection

This section analyses the availability of stars as the angular velocity increases. First, the review of the stars distribution over the celestial sphere is presented considering modern star catalogs. Then, the theoretical calculation of the expected number of stars as a function of the angular velocity is discussed.

4.1. Stars distribution in the on-board catalog

IMPA requires an on-board catalog based on the Hipparcos identifier and the magnitude of two stars. These information have been collected from the

Hipparcos stars catalog provided by ESA[5] and they have been also adopted to simulate stars' positions on the celestial sphere. The full catalog contains 118,218 stars with several information for each celestial body. The required values for the simulations are:

- Hipparcos identifier h
- Right Ascension α
- Declination δ
- Magnitude m

The identifier is an integer number ranging from 1 to 120416. Right ascension and declination are expressed in degrees for epoch J1991.25 in the International Celestial Reference System (ICRS). The cataloged magnitude is in the interval $[-1.44, 14.1]$.

To limit the memory requirement and increase the research efficiency, the stars within the on-board catalog must satisfy two requirements: the angle between every couple of stars must be less than a maximum angle θ_M depending on the field of view's (FOV) dimension, and the stars' magnitudes must be less than the maximum detectable magnitude m_M.

The m_M value depends on the segmentation detection threshold τ_{pre} (see Sec. 2.1) and the noise contributions. Hence, a proper choice of m_M depends on the specific technological device taken into account. In this paper, m_M is considered equal to 5.5, in accordance with the optical characteristics of commercial star trackers. Stars with magnitudes greater than m_M are not included in the on-board catalog. Nonetheless, they are considered for the sky simulation as they can eventually appear as false objects. Indeed, a faint star can be detectable if the noise signal increases the energy value of the pixels belonging to the star.

Let h_{l1} and h_{l2} be the indexes of a couple of stars with magnitude m_{l1} and m_{l2}, and $\theta_l \geq 0$ be the angular distance between the two stars. The on-board catalog F is an ordered set composed by four-elements sets $\{h_{l1}, h_{l2}, m_{l1}, m_{l2}\}$, satisfying the requirements $\theta_l \leq \theta_M$, $m_{l1} \leq m_M$, $m_{l2} \leq m_M$ i.e.

$$F = \{ f_l = \{h_{lk}, m_{lk}\} : \theta_l \leq \theta_{l+1} \leq \theta_M, m_{lk} < m_M,\ k = 1, 2,\ 1 \leq l \leq N_F \}\,, \quad (23)$$

[5] http://www.cosmos.esa.int/web/hipparcos

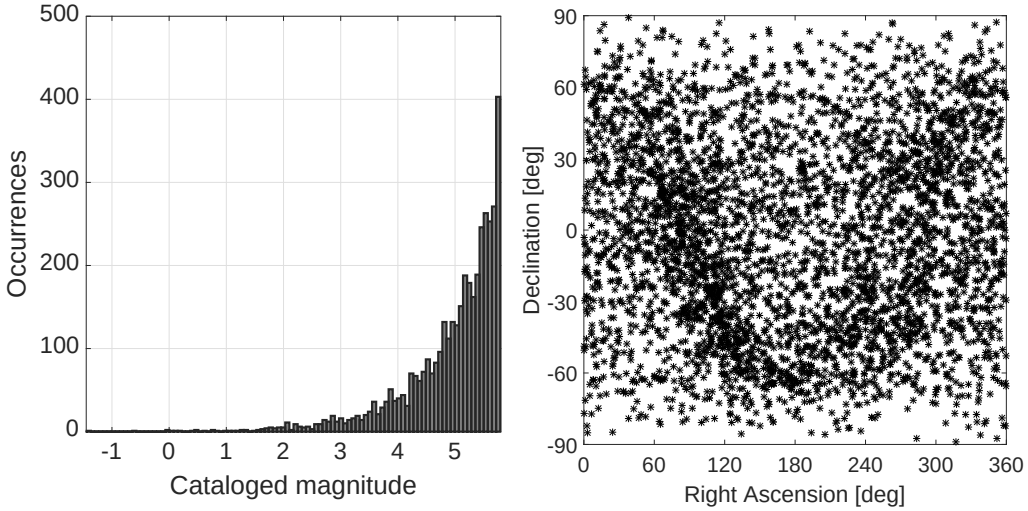

(a) (b)

Figure 5: On-board catalog distribution with respect to cataloged magnitude (a) and in the plane Right Ascension and Declination (b).

where N_F is the number of stars couples satisfying the constraints. Note that the angle θ_l is not explicitly included in the on-board catalog F as it is recovered by means of the K-vector searching technique employed by the stars recognition algorithm (see Sec. 5.2).

Fig. 5a reports the distribution of magnitudes of the stars in the on-board catalog. The number of stars is reduced with respect to the full catalog (from 118,218 stars in the full catalog to 3,349 stars in the on-board catalog). Fig. 5b shows the stars' positions expressed as Right Ascension and Declination. As can be seen, the sky is not covered in an isotropic way due to the presence of very bright stars in the Milky Way.

4.2. Star detection in dynamic conditions

When the stars move in the focal plane due to non-negligible angular velocities, the star's signal is spread over more pixels with respect to the stationary case. As a consequence, the number of photoelectrons associated to the single pixel of a streak in dynamic conditions is smaller than the number of photoelectrons associated to the pixel of a spot in stationary case. When the number of photoelectrons is too small, the star signal can be too

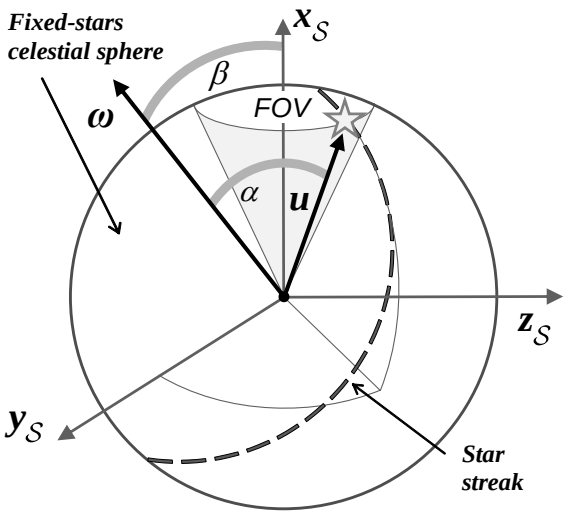

Figure 6: Star position and angular velocity vectors in the sensor reference frame.

low to pass the threshold τ_{pre} of the preprocessing (see Sec. 2.1). Hence, with increasing angular velocities, the number of detected stars usually decreases. This problem has been already investigated in different works, e.g. [14, 15].

With reference to Fig. 6, the nominal arc-length l of a star in the focal plane is expressed as

$$l = \sin(\alpha)\,\omega\Delta t, \tag{24}$$

where $\Delta t = T_{exp}$ for a global shutter detector and $\Delta t = T_{exp} + s_z\Delta T$ for a rolling shutter detector. The angle between the angular velocity vector and the star in the FOV is denoted as α. If $\alpha = 0$ then the star appears as a spot regardless of the angular velocity's magnitude and the value taken on by β. Eq. (24) is valid as long as the angular acceleration is negligible. The arc-length is maximum when $\alpha = 90$ deg, and the arc becomes a straight line of length $l = \omega\Delta t$.

In this section, a model which is very close to the one presented in [14] is considered, as well as already done in [16]. In stationary conditions, a star with magnitude zero is associated to a signal flux intensity denoted as G_0, measured in e^-/s, which represents the number of photoelectrons emitted by a star of magnitude 0 during an exposure time of one second. If a square detector with n_{pixel} per side is considered, and the instantaneous field of view

(IFOV) is defined as

$$\text{IFOV} = \frac{\text{FOV}}{n_{pixel}}, \tag{25}$$

the number of covered pixels in dynamic conditions is given by

$$n_{cov} = \frac{r_{psf} l}{\text{IFOV}}. \tag{26}$$

In Eq. (26), r_{psf} is a constant parameter related to the point spread function (PSF) of the detector. The PSF describes the response of the detector to the star signal, i.e. the spread of the star signal over several pixels.

Finally, the number of photoelectrons associated to a zero magnitude star in dynamic conditions is given by

$$I_0 = \frac{G_0 \Delta t}{n_{cov}}, \tag{27}$$

and considering Eq. (26) and l as given by Eq. (24),

$$I_0 = \text{IFOV} \frac{G_0}{r_{psf} \sin(\alpha)\, \omega}. \tag{28}$$

The threshold condition for a star to be detected is that its signal I_{th} is equal to τ_{pre}. Hence, using the Pogson's formula

$$m_0 - m_{th} = -2.5 \log_{10} \left(\frac{I_0}{I_{th}} \right), \tag{29}$$

the reference threshold magnitude can be evaluated as

$$m_{th} = 2.5 \log_{10} \left(\frac{I_0}{I_{th}} \right) \tag{30}$$

since $m_0 = 0$. The results of this analytical model are reported in Sec. 6, where the specific features and noises of the sensor considered in this work are used, and they are compared with the results from the numerical simulator.

5. Star Identification Algorithm

The star identification approach proposed in this work is the Improved Multi-Poles Algorithm (Improved MPA, or IMPA), a method based on polar techniques features and internal verification phases guaranteeing good reliability in the presence of false objects.

The original version of MPA [21] was based on three phases: *acceptance, verification* and *confirmation*. The algorithm was validated considering stable attitudes and very slow angular rates up to 0.15 deg/s. In stable attitude the results have shown a success rate of 100 %, when considering sets of input objects with up to 185 false objects and 33 cataloged stars. The success rate decreased at 66 % in the simulated worst case with 486 false objects and 31 cataloged stars.

A revised version of the MPA has been proposed to participate at the European Space Agency (ESA) competition "Star Trackers: First Contact". The introduction of a *magnitude filtering* is the principal improvement with respect to the original method, leading to a simplification of the algorithm architecture since the confirmation phase is not required anymore. Results of the revised MPA are reported in [22], where the high efficiency, reliability and small computational effort are proven to be core characteristics of the algorithm.

The IMPA is an approach based on the features of the two former algorithm versions, with a simplified check phase in comparison to the one reported in [22]. Furthermore, an enhanced robustness to angular rates has been accomplished by adopting a greater searching tolerance (feasible thanks to the introduction of magnitude filtering). Finally, when using detectors based on rolling shutter, the compensation of rolling shutter effects is required. The most important characteristics of the proposed method are described in the following paragraphs.

5.1. Improved Multi-Poles Algorithm

The IMPA input is the list of clusters that can represent either true stars or artifacts. Each cluster is characterized by the centroid coordinates $\boldsymbol{c} = [c_y, c_z]^T$ and a detected signal intensity value $E_{\mathscr{C}}$. Centroids are two-dimensional vectors associated to dense sets of pixels, recognized from the clustering operation as potential signals associated to stars (refer to Sec. 2.2). In the following description, the tilde ($\sim$) symbol above a letter will be used to distinguish a quantity measured using the image information from

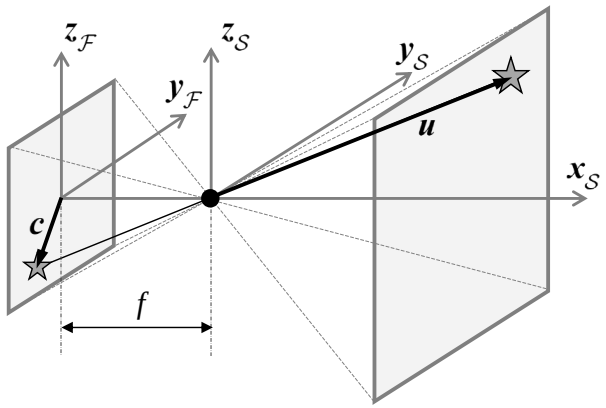

Figure 7: Sensor and focal plane reference frames.

the same reference catalogued quantity, which has a different value from the measured one.

First of all, the unit vector $\boldsymbol{u}$ in the sensor's reference frame $\mathcal{S} \subset \mathbb{R}^3$ is evaluated according to Eq. (31) for each cluster. With reference to Fig. 7, the unit vector $\boldsymbol{u}$ points to a star within the field of view of the star tracker. Its coordinates are related to the projected coordinates in the focal reference frame $\mathcal{F} \subset \mathbb{R}^2$ of the centroid $\boldsymbol{c} = [c_y, c_z]^T$ by

$$\boldsymbol{u} = \frac{1}{\sqrt{c_y^2 + c_z^2 + f^2}} \begin{bmatrix} f \\ -c_y \\ -c_z \end{bmatrix}. \tag{31}$$

There are other more sophisticated models different from the simple pinhole camera one, given in Eq. (31) [29]. However, as long as the image from a star tracker is properly modeled and calibrated, the camera model does not strongly affect the star recognition algorithm performances.

To estimate the magnitude value from the detected signal intensity, the adopted model is derived from the Pogson's formula already used in Eqs. (29) and (30). i.e.

$$\tilde{m}_i = -2.5 \cdot \log_{10} \left(\frac{E_{\mathscr{C}_i}}{G_0 \cdot T_{exp}} \right). \tag{32}$$

The magnitude value will be different from the cataloged one, since the signal intensity value is affected by the noise sources' contributions.

Each cluster in the image is associated to a 4 dimensional vector $\boldsymbol{s}$ named *spike* collecting the unit three-dimensional vector $\boldsymbol{u}$ and the estimated magnitude value $\tilde{m}$, i.e.

$$\boldsymbol{s} = [\boldsymbol{u}, \tilde{m}]. \tag{33}$$

It is noteworthy that for APS sensors with rolling shutter, $\boldsymbol{u}$ is evaluated with Eq. (31) after the compensation given by Eq. (21) is applied. The list containing all the spikes sorted by ascending magnitude is defined as the following ordered set

$$S = \{\boldsymbol{s}_i = [\boldsymbol{u}_i, \tilde{m}_i] \in \mathbb{R}^4, \text{ with } \tilde{m}_i < \tilde{m}_{i+1} \text{ for } i = 1, ..., N_s\} \tag{34}$$

where N_s is the number of spikes in the image.

The IMPA identifies the stars using two phases: the *acceptance phase* and the *check phase*. The acceptance phase exploits the approach of a polar technique to yield a set of elements, named *accepted stars*, which are selected among the objects in the image. In an ideal case, with no noises and false objects, the set of accepted stars is the set of the *recognized stars*. In the real case, especially in a harsh environment, some false objects can be accepted as stars. For this reason, the check phase performs a cross-check between two sets of accepted stars to control which elements have been detected in both sets.

Consequently, at the initial step of the IMPA, the acceptance phase has to run at least twice. If a set of accepted stars is returned, the next pole is selected within the previous accepted neighbor stars, since the magnitude filtering drastically reduces false object acceptation. The cross-check is based on a check on the number of stars belonging to both the sets. If this number is less than a desired number of recognized stars, the algorithm goes back to the acceptance phase in order to yield a new independent accepted stars set. On the contrary, the stars belonging to both sets are returned by the algorithm as *recognized stars*.

For the sake of clarity, in the following explanation the two phases are described using illustrative figures with a set S of eight elements (see Fig. 8). The figures depict only the mechanism of how the algorithm works, while the results with the real number of objects are presented in Sec. 6. Spikes are represented as circles with the radius related to the magnitude, i.e. the brightest object is the one with the greatest diameter.

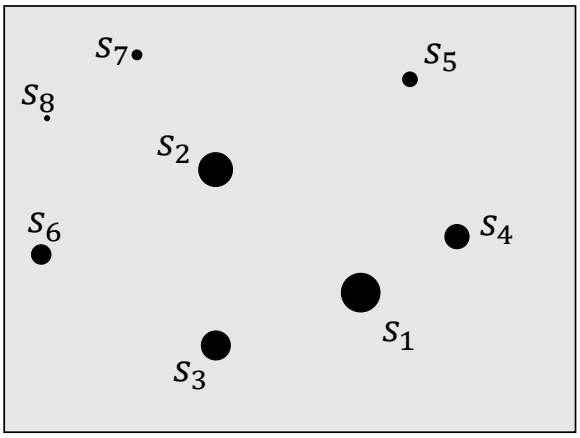

Figure 8: Set S with eight elements.

5.2. Acceptance phase

At the i^{th} run, the acceptance phase selects in S the *pole* $\boldsymbol{p}^{(i)}$ and the *neighbors* $\boldsymbol{n}_j^{(i)}$ as

$$\begin{aligned} \boldsymbol{p}^{(i)} &= \boldsymbol{s}_i, \quad i \in \{1, ..., N_s\}, \\ \boldsymbol{n}_j^{(i)} &= \boldsymbol{s}_j, \quad \forall j \in \{1, ..., N_s\},\ j \neq i. \end{aligned} \tag{35}$$

Recalling the spikes definition in Eq. (33), the angular distances $\tilde{\theta}_{ij}$ between the *pole*, with direction $\boldsymbol{u}_i$, and the j^{th} *neighbor*, with direction $\boldsymbol{u}_j$, is computed as

$$\tilde{\theta}_{ij} = \arccos(\boldsymbol{u}_i \cdot \boldsymbol{u}_j). \tag{36}$$

The first pole is chosen as $\boldsymbol{s}_1$, i.e. the spike with minimum magnitude as depicted in Fig. 9, where the dotted lines represent the angular distances from the pole to the neighbors. This criterion reduces the risk of false matching and recognition, since cataloged stars with magnitude in the neighborhood of m_1 are generally far less than the cataloged stars with magnitude in the neighborhood of m_2 if $m_1 < m_2$ (see Fig. 5a).

For each computed angular distance $\tilde{\theta}_{ij}$, the specific features f_l are searched in F with values θ_l such that $|\theta_l - \tilde{\theta}_{ij}| \leq \varepsilon_\theta$, where ε_θ is a user-defined tolerance. This is a range searching problem solved using the K-Vector technique [30]. The selection of the suitable value of ε_θ is strongly affected by the sensor's operative conditions and by the environmental noises. Recalling the definition of the catalog given in Eq. (23), the result of the search leads to

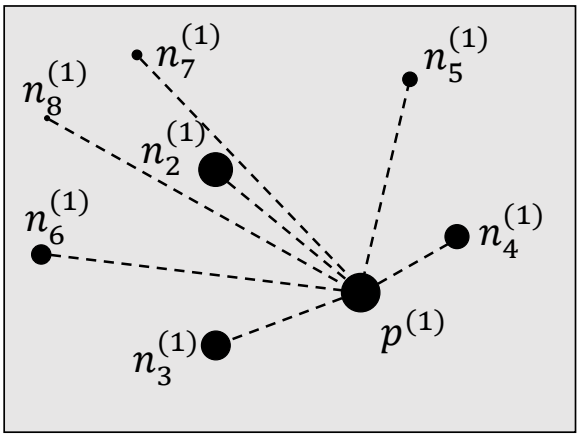

Figure 9: First Pole selection

identify the subset $F_K^{(i,j)} \subset F$ given as

$$F_K^{(i,j)} = \{f_l \in F : |\theta_l - \tilde{\theta}_{ij}| \leq \varepsilon_\theta\}. \tag{37}$$

The superscript (i, j) denotes that the i^{th} spike is the *pole* while the j^{th} spike is the *neighbor*. To make the searching algorithm more efficient, the magnitude information is used to restrict the number of cataloged stars associated with the elements in $F_K^{(i,j)}$. Indeed, only the stars with cataloged magnitude similar to the estimated magnitude $\tilde{m}$ of the image spikes are considered. The magnitude feasibility is evaluated through a threshold ε_m by means of two inequalities, i.e.

$$\begin{aligned} |m_{l1} - \tilde{m}_i| < \varepsilon_m \quad &\wedge \quad |m_{l2} - \tilde{m}_j| < \varepsilon_m \\ &\text{or} \\ |m_{l2} - \tilde{m}_i| < \varepsilon_m \quad &\wedge \quad |m_{l1} - \tilde{m}_j| < \varepsilon_m \end{aligned} \tag{38}$$

where the symbol $\wedge$ is the logical "and" operator. The candidate stars are now contained in the subset $F_{Km}^{(i,j)} \subset F_K^{(i,j)} \subset F$ defined as

$$F_{Km}^{(i,j)} = \{f_l \in F_K : \text{Eq. (38) is satisfied}\}. \tag{39}$$

The identifiers of stars pairs contained in $F_{Km}^{(i,j)}$ are then stored in the set defined as

$$\Pi^{(i,j)} = \{\pi_l^{(i,j)} = \{h_{l1}, h_{l2}\},\ l : f_l \in F_{Km}^{(i,j)}\}. \tag{40}$$

Applying the described procedure to all the *neighbors* of the i^{th} spike, we obtain $(N_s - 1)$ subsets $\Pi^{(i,j)}$. The set $\Pi^{(i)}$ with elements $\pi_l^{(i)}$ is defined as the union of the subsets $\Pi^{(i,j)}$, i.e.

$$\Pi^{(i)} = \bigcup_{j\,|j\neq i}^{N_s} \Pi^{(i,j)}. \tag{41}$$

The star identifier which has the maximum occurrence within the elements of $\Pi^{(i)}$ is selected as the pole identifier $p^{*(i)}$. If $p^{*(i)}$ is a unique value, then it may be associated to the pole star $\boldsymbol{p}^{(i)}$ and the pole is accepted. On the contrary, the pole is not accepted if more than one identifier has the maximum number of appearances. Accordingly, when there are only 2 actual stars in the image, the algorithm cannot identify them. In fact, the occurrence of Hipparcos identifier for the actual star is 1 even if it is selected as a pole.

Once the pole star is accepted, $p^{*(i)}$ does actually represent either h_{l1} or h_{l2} for n different elements $\pi_l^{(i)}$ in $\Pi^{(i)}$, where $n \leq (N_s - 1)$. That is, $p^{*(i)}$ has been found in one element of n different sets $\Pi^{(i,j)}$. For the couples $\{\boldsymbol{n}_j^{(i)}, \boldsymbol{p}^{(i)}\}$, such that an element $\{h_\beta, p^{*(i)}\}$ is found in $\Pi^{(i,j)}$ ($h_\beta = h_{l1}$ or $h_\beta = h_{l2}$), the neighbor stars identifier is defined as $n_j^{*(i)} = h_\beta$. For the neighbor stars where the coupling with $p^{*(i)}$ is not found, the identifiers are marked as false (identifier equal to -1). Summing up,

$$n_j^{*(i)} = \begin{cases} h_\beta & \text{if } \{h_\beta, p^{*(i)}\} \in \Pi^{(i,j)}, \\ -1 & \text{otherwise.} \end{cases} \tag{42}$$

As a result, the set of the accepted stars $A^{*(i)}$ can be defined as

$$A^{*(i)} = \{p^{*(i)}, n_j^{*(i)},\ j = 1, ..., N_s \quad \text{with} \quad j \neq i\}. \tag{43}$$

When the pole star is identified, the N_s-long set $A^{*(i)}$ contains the hipparcos identifiers of the accepted stars and the false marker for the others (see Fig. 10). In such a case, the acceptance phase runs a second time with a different selection criterion for the new pole. Indeed, new poles are selected within the spikes previously accepted as neighbor stars. The process ends as soon as two accepted stars sets $A^{*(i)}$ and $A^{*(j)}$ are obtained.

On the contrary, if the first pole cannot be identified, the set $A^{*(i)}$ contains N_s elements equals to -1, i.e. no star identifiers. In this case, the selection

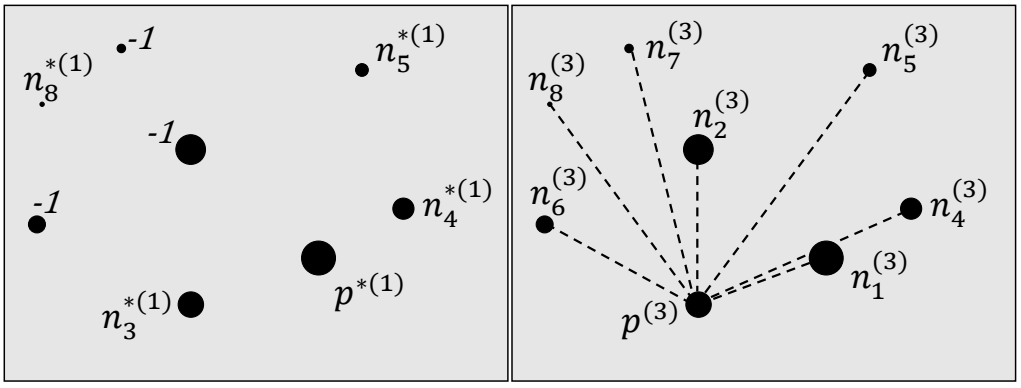

(a) (b)

Figure 10: Next pole selection when an accepted stars set has been returned.

criterion for the successive pole remains the magnitude of the spikes. Thus, the spike $\boldsymbol{s}_{i+1}$ is selected as pole $\boldsymbol{p}^{(i+1)}$ (see Fig. 11).

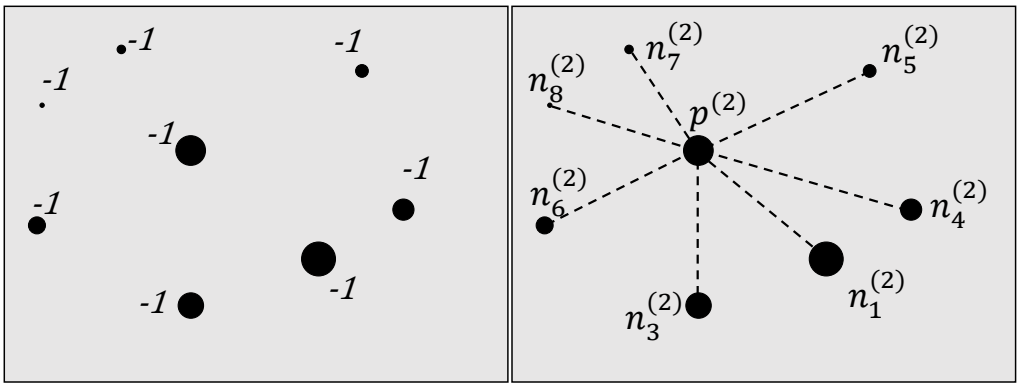

(a) (b)

Figure 11: Next pole selection when an accepted stars set has not been returned.

5.3. Check phase

The check phase verifies if the number of accepted stars belonging to the intersection of two sets $A^{*(i)}$ and $A^{*(j)}$ is greater than a user-defined threshold value t^*. This number corresponds to the minimum number of required stars and it must be greater than 2 since

- at least 3 stars are required to perform a reliable attitude determination, and
- the pole identification may be achieved only if the pole is coupled with at least 2 neighbors.

Let two sets $A^{*(i)}$ and $A^{*(j)}$ be considered. The check phase is based on the evaluation of the boolean variable ζ

$$\zeta = \begin{cases} 1 & \text{if} \quad \#\left(\{A^{*(i)} \cap A^{*(j)}\}^{+}\right) \geq t^{*}, \\ 0 & \text{otherwise,} \end{cases} \tag{44}$$

where $\#(X)$ stands for the cardinality of the set X, i.e. the number of elements belonging to X. Moreover, X^{+} is the subset containing only the positive elements of X and it is used for the definition of ζ so that the intersection does not consider the presence of the false markers. The value of the threshold t^{*} is related to the on-board catalog, sensor noises and sensor FOV.

The recognized stars set R^{*} is obtained as

$$R^{*} = \begin{cases} A^{*(i)} \cap A^{*(j)} & \text{if } \zeta = 1 \\ -1, ..., -1 \quad \forall \boldsymbol{s}_i & \text{otherwise.} \end{cases} \tag{45}$$

The elements of R^{*} can either be the stars indices of the on-board catalog in the case of true stars, or the identifier "-1" in the case of false stars. If the boolean variable ζ is never true, all the spikes in the image are marked as false stars. In this case, all the N_s elements within the returned R^{*} set are "-1".

A noteworthy comment about the value of t^{*} is in order. The spacecraft angular motion affects the acquisition of the sky image so that faint stars are more difficult to be detected with respect to the stationary attitude. Indeed, the angular velocity affects the distribution of a star's energy on the detector reducing the value of the signal on the single pixels. As a result, the image preprocessing can discard some of the real stars because of the low signal to noise ratio. This issue must be considered when setting the minimum number of stars t^{*} required for passing the check phase of the IMPA. Indeed, too low values of t^{*} reduce the robustness to false objects whereas too high values of t^{*} are not suitable with high slew rates.

6. Test Definition and Results

A reliable simulator is required in order to obtain accurate numerical results while testing the rolling shutter compensation strategy and the IMPA. To this end, the high fidelity simulator and noise sources described in [21] have been adopted in this work. The main characteristics of the simulator and noises are summarized in Table 1 and Table 2 respectively.

Table 1: Main characteristics of the Simulator.

Sensor characteristic	Adopted value
Detector	1024 × 1024 Active Pixel Sensor (APS)
Field of View (FOV)	20 × 20 deg
Focal length f	52 mm
Exposure time T_{exp}	0.2 s
Pixel dimensions	18 × 18 µm
Simulated stars magnitude $\mathcal{M}_S$	$\mathcal{M}_S \leq 6.5$
On-board catalog	Hipparcos stars with $\mathcal{M}_C \leq 5.5$
G_0	7300000 e^-/s
τ_{pre}	500 e^-
d_f	2 pixel

Table 2: Main characteristics of noise sources.

Noise sources	Adopted model
Dark current	Normal distribution: 100 e^- mean and 5 e^- std [31].
Stray-light	Uniform value of 6000 e^- over the whole detector.
Shot noise	Poisson probability distribution proportional to the square root of the detected signal[32].
Read-out noise	Normal distribution: 0 mean and 50 e^- std [33].

6.1. Detection analysis

The results of the detection analysis described in Sec. 4.2 are here reported. The value of r_{psf} has been set equal to 3 to be consistent with the mean value of the PSF used in the high fidelity simulator. In Fig. 12 the

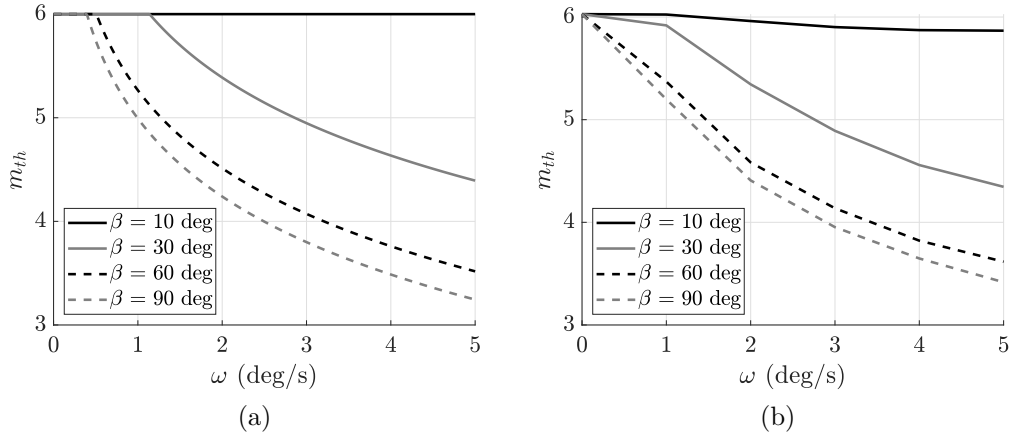

Figure 12: Maximum detected magnitude from Liebe model (a) and from simulation campaigns (b) as a function of the angular velocity magnitude and direction.

expected results from the mathematical model are compared with the results from the simulator. As can be seen, there is a good matching between the two families of curves. It is to be noted that the results are reported as a function of the angle β, as this angle can be easily set in the simulator. The analytical results are obtained considering $\alpha = \beta - 0.5\,\mathrm{FOV}$, as this is the kinematic geometry ensuring the best detection conditions. The analytical results have been reported considering a maximum detectable magnitude equal to 6 (indeed, the analytical model does diverge near $\omega = 0$). These results justify the maximum magnitude considered in the on-board catalog reported in Table 1. In fact, this value is a good trade-off between having a reduced catalog in terms of required allocation memory, and having the minimum number of stars both in stationary and dynamic conditions.

It is noteworthy that, at low angular rates, stars with magnitude higher than 5.5 are detected. Since these stars are not reported in the on-board catalog, they are treated as false objects which are taken into account without problems by the IMPA.

6.2. IMPA setting and test campaigns definition

The purpose of the performed tests has been to verify that the proposed algorithm can give reasonable results in the range of angular velocities between 1 deg/s and 5 deg/s, and in the presence of a high number of false objects. The test campaigns have been carried out considering:

1. $N_\omega = 5$ constant angular rates, with $\omega = 1, ..., 5$ deg/s.
2. $N_{att} = 200$ different attitudes obtained sampling uniformly the whole celestial sphere considering the celestial sphere approximated by a geodesic polyhedron.
3. $N_{dir} = 26$ different relative orientations between the angular velocity vector and the sensor's boresight. The directions of the angular velocity have been obtained as the combination of $-1, 0, 1$ along each coordinate of the angular velocity vector expressed in $\mathcal{S}$, with successive normalization.

Considering the different rates, attitudes and angular velocity directions, a total of 26,000 simulations have been run. Moreover, additional 200 simulations have been considered for the reference test case with $\omega = 0$ deg/s.

Global and rolling shutter acquisition architectures have been considered for testing the IMPA. Two test campaigns have been performed for both types of detector:

Best-case condition: The star-tracker is tested for increasing angular rates in the presence of a low number of false objects identified as the uncatalogued stars in each images.

Worst-case condition: The star-tracker is tested for increasing angular rates in the presence of a high number of false objects, including uncatalogued stars, spots from SEUs and other noise sources.

The simulation ends when the attitude is returned reporting the number of required images. The following hypotheses have been considered:

- The maximum number of consecutive images is set to $N_{im} = 60$. When the simulation ends after the 60th image has been processed, the attitude is considered as not returned.
- The minimum number of required images is 2, since the lost in space problem is generally required to give at least a rough estimation of the angular velocity. When considering rolling shutter effects, moreover, two images are required to perform the compensation.

The attitude determination is performed applying the q-method [34] to the *recognized stars*. Results are obtained defining a tolerance on the maximum absolute error of pitch and yaw angles, since this condition ensures the capability to switch to the tracking mode. Accordingly, a simulation is *successful*

if the IMPA and q-method give errors within 360 arcsec. In the opposite case, the result is considered *not successful*. Numerical tests have shown that the occurrence of *no success* never happens, demonstrating that 1) the rolling shutter compensation works properly and 2) the check phase blocks wrong matchings.

The searching tolerance value considered for the simulations is set to 100 arcsec, equals to 3 times the standard deviation value after rolling shutter compensation for $\omega = 5$ deg/s (see Table 4). This value will guarantee the availability of star identification also in the presence of high slew rates. As a trade-off between robustness to angular rates and robustness to false objects, the t^* value has been set to 5 stars.

6.3. Compensation results

The position error due to the rolling shutter is denoted as ϵ^{RS} and it is evaluated along the horizontal and vertical directions as

$$\epsilon_y^{RS} = \tilde{c}_y - c_y^*, \quad \epsilon_z^{RS} = \tilde{c}_z - c_z^*, \tag{46}$$

where $\{c_y^*, c_z^*\}$ is the real position of the star centroid (not affected by noise, quantization, segmentation, etc.). The symbols $\tilde{\epsilon}_y^{RS}$ and $\tilde{\epsilon}_z^{RS}$ will be adopted when the compensated centroids $\{\tilde{c}_y, \tilde{c}_z\}$ are used. In an analogues way, the position errors using global shutter architecture is denoted as ϵ^{GS}.

Fig. 13 reports the position errors' distributions with global shutter, and the results of the rolling shutter compensation with angular velocity equal to 5 deg/s. Fig. 13a and 13b show the distribution of the centroids' position errors using global shutter. In Fig. 13c and 13d the components of the centroids' position errors with compensation are shown. The maximum errors with rolling shutter compensation can be compared with the maximum errors found with global shutter,even though the distributions are very different. The centroids position's errors without rolling shutter compensation are reported in Fig. 13e and 13f. As can be seen, the compensation reduces the dispersion of the errors by about one order of magnitude, concentrating almost all the results below an absolute error of 2 pixels. On the other hand, errors without compensation can reach values close to 20 pixels.

Similar results are obtained for intermediate angular rates. Table 3 reports the mean value, standard deviation, skewness and kurtosis of the centroids errors' distributions with global shutter. Table 4 and 5 report the characteristics of the centroids errors' distributions with and without the

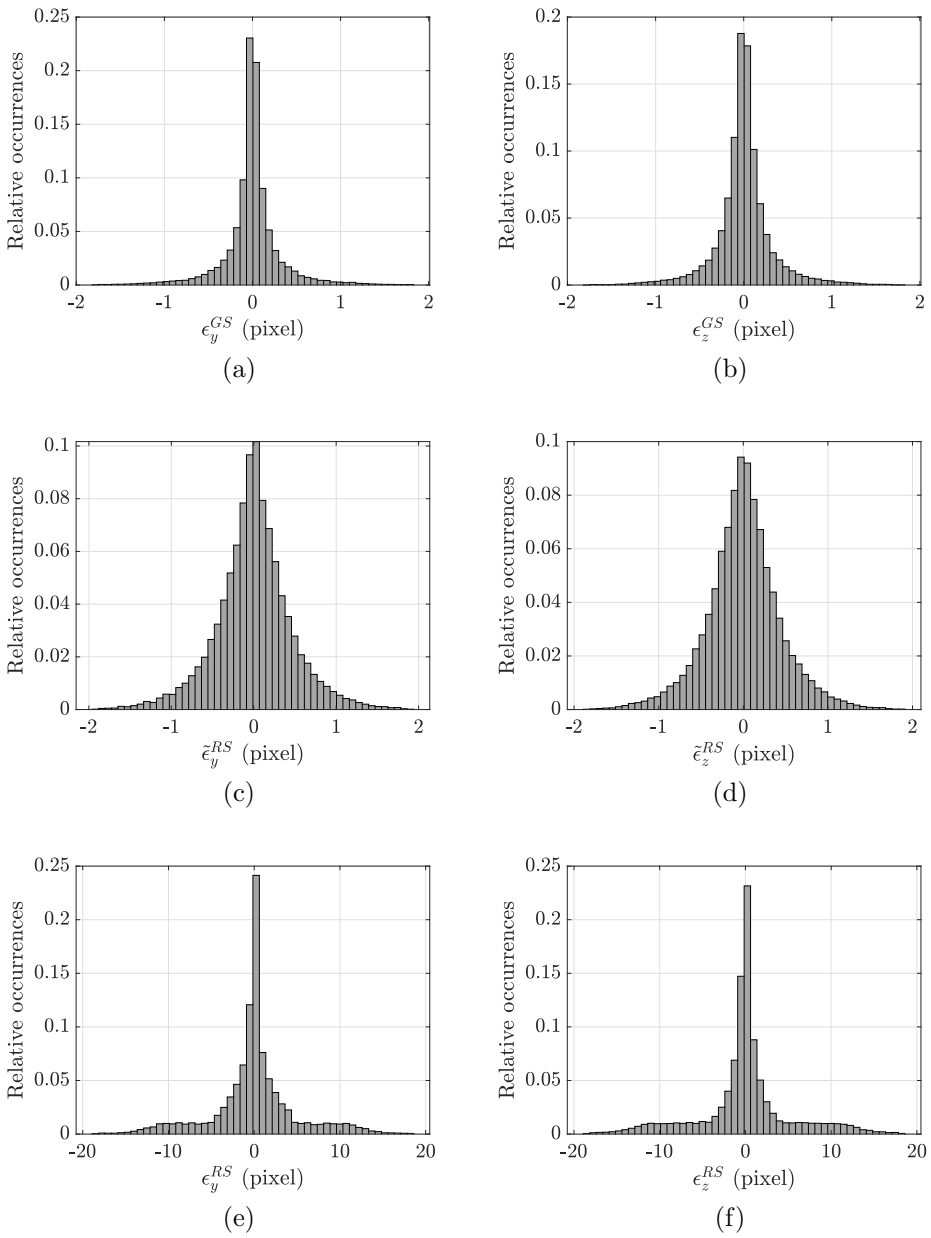

Figure 13: Centroid errors at $\omega = 5$ deg/s with global shutter (a-b) and rolling shutter with compensation (c-d) and without compensation (e-f).

Table 3: Centroid displacement errors with global shutter.

Angular rate (deg/s)	mean value (pixel)	stand. dev. (pixel)	skewness (pixel)	kurtosis (pixel)
	Horizontal displacement error, ϵ_y^{GS}			
1	-1.34×10^{-4}	1.65×10^{-1}	3.13×10^{-4}	5.83
2	-1.61×10^{-3}	2.13×10^{-1}	-2.97×10^{-2}	6.56
3	-2.88×10^{-4}	2.60×10^{-1}	-1.28×10^{-2}	7.85
4	1.58×10^{-3}	2.97×10^{-1}	3.23×10^{-2}	8.83
5	-1.30×10^{-3}	3.28×10^{-1}	-4.31×10^{-2}	9.15
	Vertical displacement error, ϵ_z^{GS}			
1	3.90×10^{-4}	1.76×10^{-1}	7.15×10^{-3}	5.22
2	1.22×10^{-3}	2.13×10^{-1}	3.34×10^{-2}	5.86
3	-4.98×10^{-4}	2.54×10^{-1}	-5.63×10^{-2}	6.78
4	5.98×10^{-4}	2.88×10^{-1}	-5.36×10^{-3}	7.38
5	2.87×10^{-3}	3.23×10^{-1}	1.06×10^{-1}	7.84

Table 4: Centroid displacement errors with rolling shutter compensation.

Angular rate (deg/s)	mean value (pixel)	stand. dev. (pixel)	skewness (pixel)	kurtosis (pixel)
	Horizontal displacement error, $\tilde{\epsilon}_y^{RS}$			
1	1.73×10^{-4}	3.77×10^{-1}	4.38×10^{-3}	4.25
2	1.44×10^{-3}	4.29×10^{-1}	5.49×10^{-3}	3.57
3	-9.30×10^{-4}	4.41×10^{-1}	-8.36×10^{-3}	3.83
4	-2.13×10^{-4}	4.58×10^{-1}	3.80×10^{-3}	4.39
5	-7.33×10^{-4}	4.61×10^{-1}	-1.97×10^{-2}	4.51
	Vertical displacement error, $\tilde{\epsilon}_z^{RS}$			
1	-1.14×10^{-3}	3.44×10^{-1}	-3.64×10^{-3}	4.15
2	1.61×10^{-4}	3.85×10^{-1}	-1.74×10^{-3}	3.82
3	-8.40×10^{-4}	4.04×10^{-1}	2.19×10^{-3}	3.91
4	-2.99×10^{-3}	4.29×10^{-1}	-1.42×10^{-2}	4.30
5	2.85×10^{-3}	4.40×10^{-1}	2.19×10^{-3}	4.34

Table 5: Centroid displacement errors without rolling shutter compensation.

Angular rate (deg/s)	mean value (pixel)	stand. dev. (pixel)	skewness (pixel)	kurtosis (pixel)
	Horizontal displacement error, ϵ_y^{RS}			
1	6.07×10^{-4}	1.52	-2.57×10^{-4}	3.04
2	4.01×10^{-3}	2.61	-2.26×10^{-3}	3.66
3	-3.97×10^{-3}	3.39	4.86×10^{-3}	4.26
4	1.57×10^{-2}	4.11	2.66×10^{-4}	4.85
5	-1.25×10^{-2}	4.87	-1.01×10^{-3}	5.05
	Vertical displacement error, ϵ_z^{RS}			
1	1.38×10^{-3}	1.54	-7.48×10^{-5}	2.99
2	1.43×10^{-2}	2.71	7.73×10^{-3}	3.54
3	1.19×10^{-3}	3.61	-2.85×10^{-3}	4.16
4	-7.85×10^{-3}	4.41	1.13×10^{-2}	4.71
5	-1.68×10^{-2}	5.25	-1.50×10^{-2}	4.93

rolling shutter compensation, respectively. The different distributions between global and compensated rolling shutter are confirmed by the kurtosis value, which in the former case is about two times the value of the latter. The standard deviation of the results after compensation is always below 0.5 pixel for each tested angular rate, which is below 35 arcsec considering the detector characteristics in Table 1. On the contrary, the standard deviation of the centroids' errors without compensation reaches 5 pixels, which is more than 350 arcsec, i.e. one order of magnitude higher than the compensated case. It can be noted that the proposed compensation strategy can slightly reduce also the mean values of the centroids' errors.

The centroids' errors values are also shown in Fig. 14, where the results using global shutter (Fig. 14a and 14b) can be compared with the results using rolling shutter with compensation (Fig. 14c and 14d) and without compensation (Fig. 14e and 14f). The improvements already shown for 5 deg/s are confirmed for all the tested rates.

6.4. Best-case IMPA results

The aim of these simulations is to evaluate the IMPA robustness to slew rates. The uncatalogued stars in each image represent the simulated false

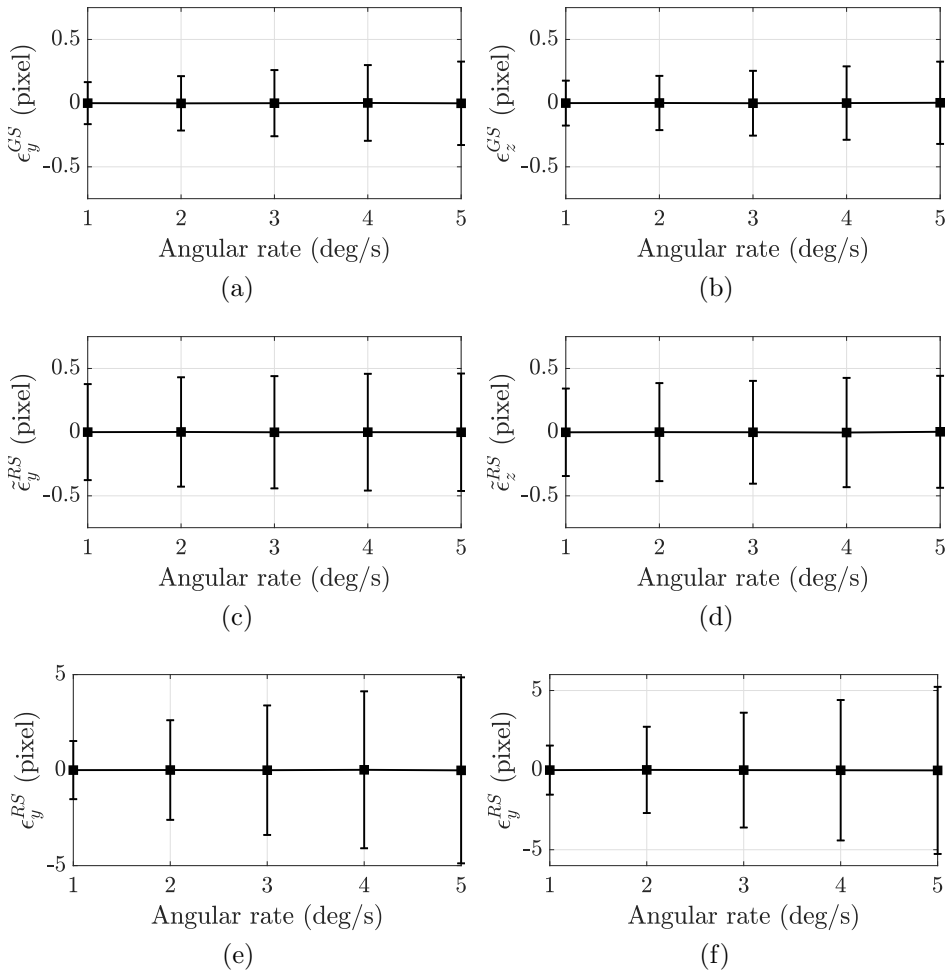

Figure 14: Errorbar plots showing centroids mean and standard deviation (1-σ) for global shutter (a-b), rolling shutter with compensation (c-d) and without compensation (e-f).

objects for this test campaign. All the rolling shutter results are considered after the deformation's compensation.

Figure 15 reports the distributions of the errors of roll, pitch and yaw angles for $\omega = 5$ deg/sec and considering global and compensated rolling shutter. It can be seen that the errors are very small and their distributions are well-fitted by Gaussian curves. Similar error distributions are obtained for the other simulations with mean and standard deviation as reported in Table 6 and Table 7.

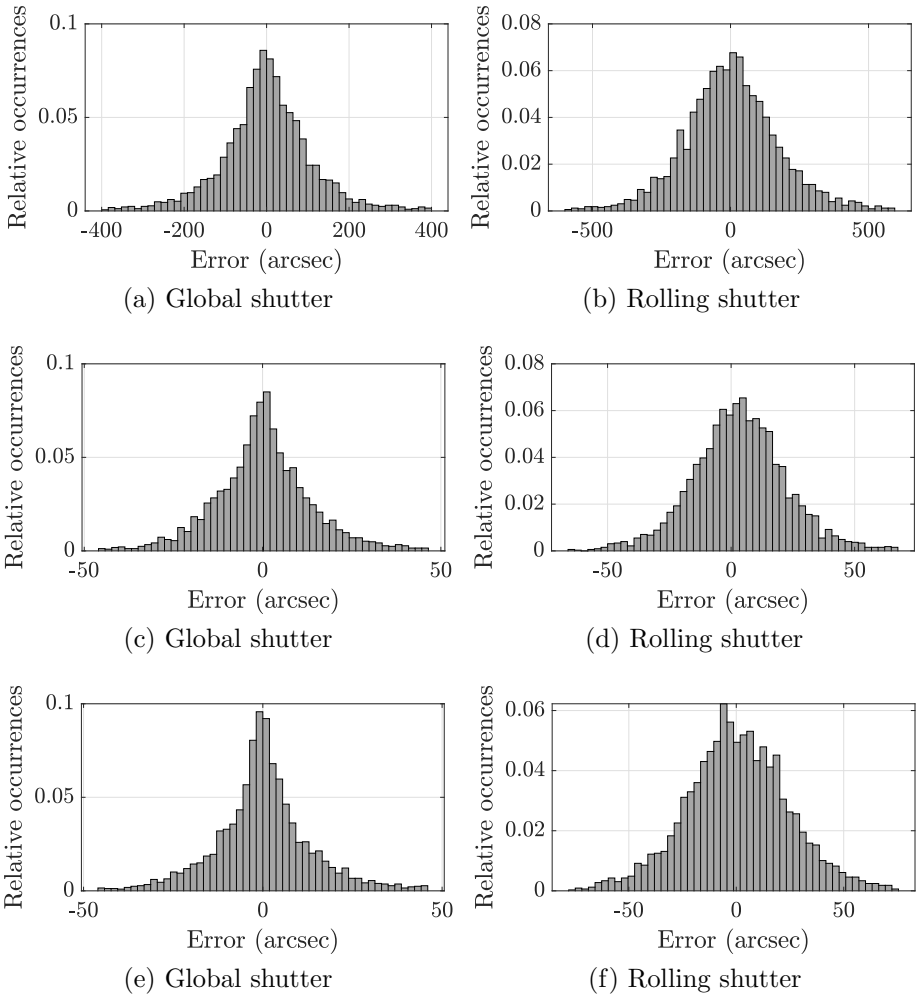

Figure 15: Best-case roll (a,b), pitch (c,d) and yaw (e,f) angle attitude errors with 5 deg/s rate

As can be seen, the standard deviation for errors' distributions depends on the rate condition. Making a comparison between the different acquisition architectures, the standard deviations are more or less the same for the test case in statical conditions. On the contrary, in the case of dynamic conditions, standard deviations with rolling shutter are of the order of two times the standard deviations obtained with global shutter. This result is consistent with the results showed in Section 6.3.

Table 6: Mean and standard deviations of attitude errors in best-case with global shutter.

Angular rate (deg/s)	Attitude Errors (arcsec) Roll Angle Mean	Roll Angle Std	Pitch Angle Mean	Pitch Angle Std	Yaw Angle Mean	Yaw Angle Std
0	0.50	13.44	0.27	2.03	0.10	1.83
1	0.79	42.93	-0.01	5.50	-0.04	5.27
2	2.50	70.97	-0.05	8.14	-0.02	8.38
3	0.31	80.52	0.00	9.78	0.11	9.65
4	1.40	94.11	-0.15	11.53	0.09	12.13
5	-0.11	108.99	0.21	13.41	0.09	13.29

Table 7: Mean and standard deviations of attitude errors in best-case with rolling shutter.

Angular rate (deg/s)	Attitude Errors (arcsec) Roll Angle Mean	Roll Angle Std	Pitch Angle Mean	Pitch Angle Std	Yaw Angle Mean	Yaw Angle Std
0	0.60	15.13	0.23	2.04	-0.07	1.87
1	3.99	153.35	-0.38	15.27	0.10	12.67
2	-5.50	176.36	1.37	17.98	-0.14	19.37
3	4.96	172.27	3.06	17.66	-0.22	21.29
4	-1.64	169.35	4.03	18.75	0.24	23.10
5	-1.10	184.89	4.62	20.30	-0.02	24.30

The percentage of successful simulations with reference to the number of required images is reported in Table 8 and Table 9. The number of required images to perform star identification increases in the presence of angular rate. The reason is related to the SNR reduction for increasing angular rate, leading to a reduction of the number of detected stars per image. As can be seen, the results are very similar for the different detector's architectures:

- The totality of the simulations has provided the attitude for the test cases with 0 and 1 deg/sec rates.
- About 3% of the simulations with 2 deg/sec requires more than 60 images to perform attitude determination.
- About 15% of the simulations with 3 deg/sec requires more than 60

images to perform attitude determination.

- About 30% of the simulations with 4 deg/sec requires more than 60 images to perform attitude determination.
- About 40% of the simulations with 5 deg/sec requires more than 60 images to perform attitude determination.

Table 8: Required images for attitude determination in best-case results with global shutter.

Required images	Percentage of successful simulations [%] Angular rate (deg/s) 0	1	2	3	4	5
2	99.50	97.69	67.38	38.67	25.71	17.79
10	100.00	99.56	84.13	56.75	37.90	27.77
20	100.00	99.79	89.60	67.35	48.54	36.29
30	100.00	99.88	92.85	73.65	56.46	44.13
40	100.00	100.00	94.67	79.02	64.23	51.71
50	100.00	100.00	96.10	83.63	70.79	58.46
60	100.00	100.00	97.27	87.29	75.87	64.10

Table 9: Required images for attitude determination in best-case results with rolling shutter.

Required images	Percentage of successful simulations [%] Angular rate (deg/s) 0	1	2	3	4	5
2	98.50	98.23	63.96	34.85	22.58	16.12
10	100.00	99.73	82.29	52.75	34.00	25.02
20	100.00	99.88	88.58	62.77	43.17	33.23
30	100.00	99.94	91.94	69.67	52.12	39.79
40	100.00	100.00	93.96	75.27	58.63	46.46
50	100.00	100.00	95.58	80.02	65.40	53.10
60	100.00	100.00	96.71	84.73	70.33	58.58

6.5. Worst-case results

The aim of these simulations is to test the presented algorithm's robustness to both slew rate and the presence of false objects. The false objects have been added after the cluster fusion as objects that cannot be filtered in addition to the simulated uncatalogued stars. The added false objects are 50 for each image. Furthermore, as in the previous section, all the rolling shutter results are considered after the deformation's compensation.

As for the best-case results, errors are very small and their distributions are well-fitted by Gaussian curves. These results are reported in Table 10 and Table 11.

Table 10: Mean and standard deviations of attitude errors in worst-case with global shutter.

Angular rate	Attitude Errors (arcsec)					
	Roll Angle		Pitch Angle		Yaw Angle	
(deg/s)	Mean	Std	Mean	Std	Mean	Std
0	-0.24	16.37	0.09	1.88	0.19	2.08
1	-1.78	58.44	0.03	6.48	0.01	6.81
2	1.65	58.58	-0.08	7.40	-0.12	7.04
3	-0.87	62.11	0.10	7.60	0.14	7.71
4	0.97	75.08	0.26	8.82	-0.37	9.20
5	-2.96	102.27	0.45	11.27	-0.31	12.60

Table 11: Mean and standard deviations of attitude errors in worst-case with rolling shutter.

Angular rate	Attitude Errors (arcsec)					
	Roll Angle		Pitch Angle		Yaw Angle	
(deg/s)	Mean	Std	Mean	Std	Mean	Std
0	0.86	22.63	0.30	2.31	0.07	2.13
1	1.94	171.52	-0.09	15.53	0.03	13.64
2	-2.00	188.98	2.53	18.94	0.62	21.15
3	1.56	168.00	3.86	17.44	0.19	21.84
4	-4.44	166.59	3.22	17.56	-0.41	22.05
5	0.50	173.88	4.71	18.46	0.21	22.82

The number of required images increases in the presence of angular rate. The percentage of successful simulations with reference to the number of required images is reported in Table 12 and Table 13.

Table 12: Required images for attitude determination in worst-case results with global shutter.

Required images	Percentage of successful simulations [%] Angular rate (deg/s) 0	1	2	3	4	5
2	91.00	79.44	23.79	14.73	10.67	9.06
10	97.50	92.62	35.23	21.00	16.40	13.23
20	98.00	94.98	40.35	24.96	19.87	16.27
30	98.50	96.13	44.63	28.50	24.04	19.37
40	98.50	96.87	48.56	31.73	27.02	22.40
50	98.50	97.42	52.02	34.71	30.12	25.54
60	98.50	98.13	55.52	37.42	32.60	28.62

Table 13: Required images for attitude determination in worst-case results with rolling shutter.

Required images	Percentage of successful simulations [%] Angular rate (deg/s) 0	1	2	3	4	5
2	91.50	77.46	23.12	13.08	10.21	8.25
10	97.50	92.27	32.98	20.17	14.69	12.21
20	97.50	94.94	37.77	23.54	17.71	14.87
30	97.50	96.10	41.58	27.35	21.44	17.69
40	98.00	96.88	45.65	30.54	24.46	20.35
50	98.00	97.50	48.79	33.58	26.94	22.94
60	98.00	97.92	51.85	36.77	29.54	25.90

As can be seen, the results are very similar for the different detector's architectures:

- About 2% of the simulations with 0 and 1 deg/sec requires more than 60 images to perform attitude determination.

- About 45-48% of the simulations with 2 deg/sec requires more than 60 images to perform attitude determination.
- About 63% of the simulations with 3 deg/sec requires more than 60 images to perform attitude determination.
- About 70% of the simulations with 4 deg/sec requires more than 60 images to perform attitude determination.
- About 74% of the simulations with 5 deg/sec requires more than 60 images to perform attitude determination.

With reference to Table 8 and Table 9, the presence of false objects drastically affects the performances in terms of number of required images, reducing the performance of more than 50% at a rate of five degrees per second.

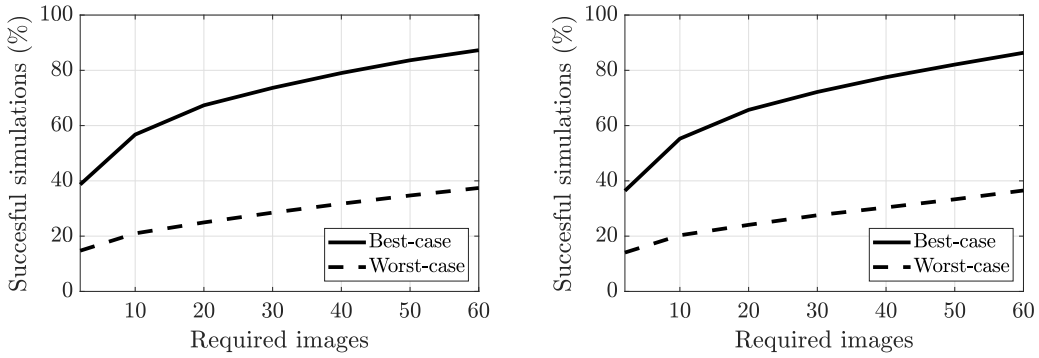

(a) Global shutter (b) Rolling shutter

Figure 16: Best-Worst cases comparison success percentage with 3 deg/sec

Figure 16 reports the trend of successful simulations versus the number of required images for the test case with 3 deg/sec, making a comparison between best and worst case. Figure 16a shows the results for global shutter architecture, while Figure 16b shows the same results for the rolling shutter case. The results are not affected by the choice between a global shutter or a rolling shutter detector. On the contrary, the performance reduction is evident between the best case and the worst case.

Figure 17 reports the trend of the successful simulations versus the angular rate in 60 images making a comparison between best and worst cases.

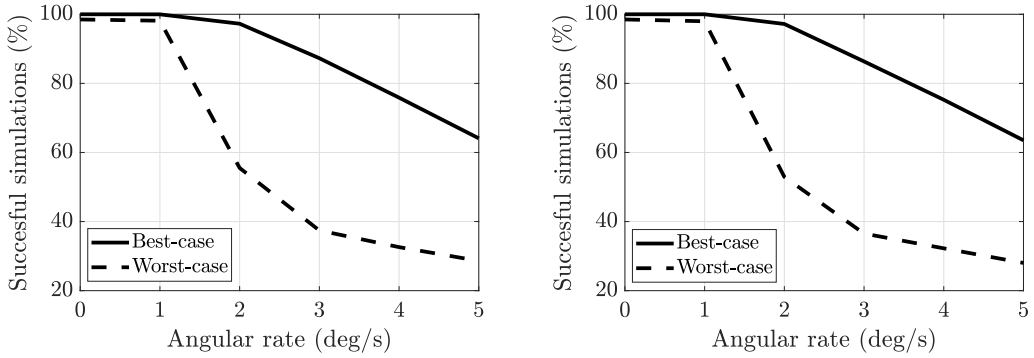

(a) Global shutter (b) Rolling shutter

Figure 17: Best-Worst cases comparison success percentage in 60 images

Figure 17a shows the results for global shutter architecture while Figure 17b shows the same results for the rolling shutter case. As for the previous results, the algorithm performances are not affected by the adopted detector but by the addition of false objects.

7. Conclusion

Through theoretical and numerical investigations, this paper has demonstrated the opportunity to use modern star tracker technology to perform accurate attitude measurements up to five degrees per second.

For detectors with rolling shutter as active pixel sensors, the deformation introduced by the read-out mode is drastically reduced by a first-order compensation model. In this way, centroiding errors with non-negligible angular rates are comparable with global and compensated rolling shutter.

The Improved Multi-Poles Algorithm has been used to take into account false objects due to electronic noises, harsh environment and non-cataloged stars. Using the proposed star recognition algorithm along with the rolling shutter compensation method, accurate and reliable attitude measurements are obtained with both global and rolling shutter detectors. Indeed, standard deviations are comparable for the test case in static conditions, whereas in dynamic conditions standard deviations with rolling shutter are of the order of two times the standard deviations obtained with global shutter. In pitch and yaw angles, standard deviations below 30 arcsec are noticed up to 5

degrees per second, whereas for the roll angle the maximum detected error is below 200 arcsec.

False objects do not significantly affect the attitude determination results. On the contrary, the number of required images for attitude determination highly depends on the number of false objects in the detected image. In fact the presence of 50 false objects drastically affects the performances in terms of number of required images, reducing the performance of more than 50% at a rate of five degrees per second. However, the IMPA is robust to false objects so that only reliable measurements are returned, since erroneous stars matching are autonomously recognized.

8. Acknowledgments

The authors would like to express their deepest appreciation to the anonymous reviser for the perceptive and valuable comments, and La Norcia Rebecca for the time that she dedicated to the linguistic support.

References

[1] C. C. Liebe, "Pattern recognition of star constellations for spacecraft applications," *Aerospace and Electronic Systems Magazine, IEEE*, vol. 8, no. 1, pp. 31–39, 1993. doi: 10.1109/62.180383

[2] C. C. Liebe, L. Alkalai, G. Domingo, B. Hancock, D. Hunter, J. Mellstrom, I. Ruiz, C. Sepulveda, and B. Pain, "Micro aps based star tracker," in *Aerospace Conference Proceedings, 2002. IEEE*, vol. 5, 2002. doi: 10.1109/AERO.2002.1035396 pp. 5–5.

[3] B. B. Spratling and D. Mortari, "A survey on star identification algorithms," *Algorithms*, vol. 2, no. 1, pp. 93–107, 2009. doi: 10.3390/a2010093

[4] C. L. Cole and J. L. Crassidis, "Fast star pattern recognition using spherical triangles," in *AIAA/AAS Astrodynamics Specialist Conference and Exhibit. Providence, Rhode Island: AIAA*, 2004. doi: 10.2514/6.2004-5389

[5] C. L. Cole and J. L. Crassidis, "Fast star-pattern recognition using planar triangles," *Journal of Guidance, Control, and Dynamics*, vol. 29, no. 1, pp. 64–71, 2006. doi: 10.2514/1.13314

[6] D. M. Gottlieb, "Star identification techniques," in *Spacecraft Attitude Determination and Control*, J. R. Wertz, Ed. Springer Netherlands, 2012, pp. 259–266. ISBN 9789400999077

[7] D. Mortari, M. A. Samaan, C. Bruccoleri, and J. L. Junkins, "The pyramid star identification technique," *Navigation*, vol. 51, no. 3, pp. 171–183, 2004. doi: 10.1002/j.2161-4296.2004.tb00349.x

[8] C. Padgett and K. Kreutz-Delgado, "A grid algorithm for autonomous star identification," *IEEE Transactions on Aerospace and Electronic Systems*, vol. 33, no. 1, pp. 202–213, 1997. doi: 10.1109/7.570743

[9] D. S. Clouse and C. W. Padgett, "Small field-of-view star identification using bayesian decision theory," *IEEE Transactions on Aerospace and Electronic Systems*, vol. 36, no. 3, pp. 773–783, 2000. doi: 10.1109/7.869495

[10] H. Lee and H. Bang, "Star pattern identification technique by modified grid algorithm," *IEEE Transactions on Aerospace and Electronic Systems*, vol. 43, no. 3, pp. 1112–1116, 2007. doi: 10.1109/TAES.2007.4383600

[11] E. Silani and M. Lovera, *Star identification algorithms: Novel approach & comparison study.* New York, Institute of Electrical and Electronics Engineers, 2006, vol. 42, no. 4.

[12] J. Xie and X. Wang, "A robust autonomous star identification algorithm for ZY3 satellite," in *2012 First International Conference on Agro- Geoinformatics (Agro-Geoinformatics).* IEEE, 2012. doi: 10.1109/Agro-Geoinformatics.2012.6311605 pp. 1–4.

[13] J. Xie, X. Tang, W. Jiang, and X. Fu, "An autonomous star identification algorithm based on the directed circularity pattern," *ISPRS - International Archives of the Photogrammetry, Remote Sensing and Spatial Information Sciences*, vol. 39, pp. 333–338, 07 2012. doi: 10.5194/isprsarchives-XXXIX-B1-333-2012

[14] C. C. Liebe, K. Gromov, and D. M. Meller, "Toward a stellar gyroscope for spacecraft attitude determination," *Journal of Guidance, Control, and Dynamics*, vol. 27, no. 1, pp. 91–99, 2004. doi: 10.2514/1.9289

[15] T. Dzamba and J. Enright, "Ground testing strategies for verifying the slew rate tolerance of star trackers," *Sensors*, vol. 14, no. 3, pp. 3939–3964, 2014. doi: 10.3390/s140303939

[16] F. Curti, D. Spiller, L. Ansalone, S. Becucci, D. Procopio, F. Boldrini, and P. Fidanzati, "Determining high rate angular velocity from star tracker measurements," in *Proceedings of the Internationa Astronautical Conference 2015*, 2015.

[17] L. Kazemi, J. Enright, and T. Dzamba, "Improving star tracker centroiding performance in dynamic imaging conditions," in *2015 IEEE Aerospace Conference*, March 2015. doi: 10.1109/AERO.2015.7119226 pp. 1–8.

[18] F. Curti, D. Spiller, L. Ansalone, S. Becucci, D. Procopio, F. Boldrini, P. Fidanzati, and G. Sechi, "High angular rate determination algorithm based on star sensing," *Advances in the Astronautical Sciences Guidance, Navigation and Control 2015*, vol. 154, p. 12, 2015.

[19] G. Berrighi and D. Procopio, "Star sensors and harsh environment," in *Spacecraft Guidance, Navigation and Control Systems*, vol. 516, 2003, p. 19.

[20] M. Kolomenkin, S. Pollak, I. Shimshoni, and M. Lindenbaum, "Geometric voting algorithm for star trackers," *IEEE Transactions on Aerospace and Electronic Systems*, vol. 44, no. 2, pp. 441–456, 2008. doi: 10.1109/TAES.2008.4560198

[21] V. Schiattarella, D. Spiller, and F. Curti, "A novel star identification technique robust to high presence of false objects: The multi-poles algorithm," *Advances in Space Research*, vol. 59, no. 8, pp. 2133–2147, 2017. doi: 10.1016/j.asr.2017.01.034

[22] V. Schiattarella, D. Spiller, and F. Curti, "Efficient star identification algorithm for nanosatellites in harsh environment," in *Advances in the Astronautical Sciences*, vol. 163, 2018, pp. 287–306.

[23] P. D. Wellner, "Adaptive thresholding for the digitaldesk - technical report EPC-1993-110," Rank Xerox Research Centre, Cambridge Laboratory, 61 Regent Street, Cambridge CB2 1AB, Tech. Rep., 1993.

[24] C. H. Messom, S. Demidenko, K. Subramaniam, and G. S. Gupta, "Size/position identification in real-time image processing using run length encoding," in *IMTC/2002. Proceedings of the 19th IEEE Instrumentation and Measurement Technology Conference (IEEE Cat. No.00CH37276)*, vol. 2, May 2002. doi: 10.1109/IMTC.2002.1007101 pp. 1055–1059.

[25] M. Sezgin and B. Sankur, "Survey over image thresholding techniques and quantitative performance evaluation," *Journal of Electronic imaging*, vol. 13, no. 1, pp. 146–166, 2004. doi: 10.1117/1.1631315

[26] R. Gonzalez and R. Woods, *Digital Image Processing*. Pearson/Prentice Hall, 2008. ISBN 9780131687288

[27] V. Rengarajan, Y. Balaji, and A. N. Rajagopalan, "Unrolling the shutter: CNN to correct motion distortions," in *2017 IEEE Conference on Computer Vision and Pattern Recognition (CVPR)*, July 2017. doi: 10.1109/CVPR.2017.252 pp. 2345–2353.

[28] C. Liang, L. Chang, and H. H. Chen, "Analysis and compensation of rolling shutter effect," *IEEE Transactions on Image Processing*, vol. 17, no. 8, pp. 1323–1330, Aug 2008. doi: 10.1109/TIP.2008.925384

[29] W. Burger and M. J. Burge, *Digital image processing: an algorithmic introduction using Java*. Springer London, 2016. ISBN 9781447166849

[30] D. Mortari and B. Neta, "K-vector range searching techniques," *Advances in the Astronautical Science*, vol. 105, pp. 449–464, 2000.

[31] J. C. Dunlap, W. C. Porter, E. Bodegom, and R. Widenhorn, "Dark current in an active pixel complementary metal-oxide-semiconductor sensor," *Journal of Electronic Imaging*, vol. 20, no. 1, pp. 013 005–1/8, 2011. doi: 10.1117/1.3533328

[32] S. V. Vaseghi, *Advanced Digital Signal Processing and Noise Reduction*. John Wiley & Sons, 2008. ISBN 9780470740163. [Online]. Available: https://books.google.it/books?id=vVgLv0ed3cgC

[33] F. Boldrini, D. Procopio, S. Airy, and L. Giulicchi, "Miniaturised star tracker (aa-str) ready to fly," in *Proceedings of The 4S Symposium Small Satellites, Systems and Services*, vol. ESA SP-571, 2004, p. 46.

[34] F. L. Markley and D. Mortari, "How to estimate attitude from vector observations," in *Proceedings of the AAS/AIAA Astrodynamics Specialist Conference*, vol. 103, no. 3, 1999, pp. 1979–1996.